Imaging Carbon Monoxide Emission in the Starburst Galaxy NGC 6000

Sergio Martín

Harvard-Smithsonian Center for Astrophysics, 60 Garden St., 02138, Cambridge, MA, USA

smartin@cfa.harvard.edu

Matthew R. George

Department of Astronomy, University of California, Berkeley, CA 94720, USA

Harvard-Smithsonian Center for Astrophysics, 60 Garden St., 02138, Cambridge, MA, USA

David J. Wilner

Harvard-Smithsonian Center for Astrophysics, 60 Garden St., 02138, Cambridge, MA, USA

Daniel Espada

Harvard-Smithsonian Center for Astrophysics, 60 Garden St., 02138, Cambridge, MA, USA

Instituto de Astrofísica de Andalucía, CSIC, Granada, Spain

ABSTRACT

We present measurements of carbon monoxide emission in the central region of the nearby starburst NGC 6000 taken with the Submillimeter Array. The $J = 2-1$ transition of ^{12}CO, ^{13}CO, and C^{18}O were imaged at a resolution of $\sim 3'' \times 2''$ ($450 \times 300\,\mathrm{pc}$). We accurately determine the dynamical center of NGC 6000 at $\alpha_{J2000.0} = 15^h49^m49\overset{s}{.}5$ and $\delta_{J2000.0} = -29°23'13''$ which agrees with the peak of molecular emission position. The observed CO dynamics could be explained in the context of the presence of a bar potential affecting the molecular material, likely responsible for the strong nuclear concentration where more than 85% of the gas is located. We detect a kinematically detached component of dense molecular gas at relatively high velocity which might be fueling the star formation. A total nuclear dynamical mass of $7 \times 10^9\,M_\odot$ is derived and a total mass of gas of $4.6 \times 10^8 M_\odot$, yielding a $M_{gas}/M_{dyn} \sim 6\%$, similar to other previously studied barred galaxies with central starbursts. We determined the mass of molecular gas with the optically thin isotopologue C^{18}O and we estimate a CO-to-H2 conversion factor $X_{CO} = 0.4 \times 10^{19}\,\mathrm{cm}^{-2}(\mathrm{K\,km\,s}^{-1})^{-1}$ in agreement with that determined in other starburst galaxies.

Subject headings: galaxies: fundamental parameters — galaxies: ISM — galaxies: kinematics and dynamics — galaxies: nuclei — galaxies: starburst — radio lines: galaxies

1. Introduction

The relation between the morphology and kinematics of the gas in the inner region of galaxies and the connection to its nuclear activity is not completely understood. Nuclear regions are often obscured by dust at optical wavelengths but can be viewed in continuum infrared dust emission as well as molecular line emission. CO can be used as a tracer of molecular gas, and its rotational transitions are observed at millimeter and sub-millimeter wavelengths. Observations of the morphology and kinematics of the molecular gas content in the central regions of spirals can provide insight into the dynamical processes occurring there (e.g., Jogee et al. 2005; Pérez-Ramírez et al. 2000). Studies indicate that instabilities in bars and dissipation of gas clouds remove angular momentum from material orbiting the galactic center, driving gas and dust inward to fuel star formation (e.g., Pfenniger & Norman 1990; Sakamoto et al. 1999; Knapen et al. 2002; Jogee et al. 2005; Sheth et al. 2005).

NGC 6000 is a nearby (D∼31.6 Mpc, Pizzella et al. 2005) barred spiral starburst galaxy. Despite its proximity and brightness, this galaxy has not been studied in as great detail as others of similar distance and luminosity, due to its southern declination. Hubble Space Telescope observations reveal several bright sources in circumnuclear star-forming rings and a large-scale ($\gtrsim 1$ kpc) bar (Carollo et al. 1997, 2002; Fathi & Peletier 2003). However, no such barred structures are identified towards the more irregular nuclear region (Carollo 1999; Hunt & Malkan 2004). Infrared observations towards the nucleus of NGC 6000 have found significant polycyclic aromatic hydrocarbon (PAH) emission (Siebenmorgen et al. 2004) and determined a dust temperature of 29.2 ± 2.6 K (Yang & Phillips 2007). NGC 6000 appears bright in CO emission (Young et al. 1995; Mauersberger et al. 1999) as well as H I (Koribalski et al. 2004) as detected with single-dish telescopes. However no detailed morphological and kinematical study of the gas content has been performed yet. A compilation of the observed and derived properties for NGC 6000 are presented in Table 1.

In this paper we present observations of the carbon monoxide emission in the $J = 2 - 1$ transition of the three brighter isotopologues (^{12}CO,^{13}CO,C^{18}O) towards NGC 6000 using the Submillimeter Array (SMA; Ho et al. 2004). This is the first high resolution morphological study of the molecular component towards NGC 6000.

2. Observations

Observations were carried out on 2007 February 20 with the Submillimeter Array (SMA) atop Mauna Kea, Hawaii. Seven out of the eight antennas of the array were operational and placed in the "compact-north" configuration, with baselines ranging $16 - 120$ m. The SIS receivers were tuned to the CO $J = 2 - 1$ frequency (230.538 GHz) in the upper side band (USB), redshifted to the NGC 6000 average systemic velocity of $2145 \, \mathrm{km \, s^{-1}}$ (Albrecht et al. 2007). The correlator was configured so that the $J = 2 - 1$ transitions of the isotopic substitutions ^{13}CO (220.398 GHz) and C^{18}O (219.560 GHz) were simultaneously observed in the lower side band (LSB). Spectral resolution was 0.8125 MHz ($\sim 1 \, \mathrm{km \, s^{-1}}$). System temperatures ranged from $125 - 250$ K, with a zenith opacity of $0.1 - 0.15$ as measured at 225 GHz from CSO.

A single field (field of view $\sim 55''$ at 230 GHz) was observed towards the central position $\alpha_{J2000.0} = 15^h 49^m 49\overset{s}{.}40$ and $\delta_{J2000.0} = -29°23'11\overset{''}{.}0$ as measured by IRAS (Sanders et al. 2003). We achieved a resolution of $2.8'' \times 1.7''$ in the uniform weighted maps and $3.7'' \times 2.2''$ in the natural weighted maps. At the distance of NGC 6000, $1''$ is equivalent to a projected distance of ~ 153 pc. Passband calibration was derived from spectra of Saturn and 3C 279. Absolute flux calibration (within a 10% accuracy) was determined from observations of Callisto. Gain fluctuations were corrected with the nearby quasar J1517-2422 at a distance of 8.7° from NGC 6000. The applied gain corrections were checked by imaging another nearby quasar, J1625-2527, at a distance of 8.9°. Data calibration and reduction was

performed using the MIR-IDL package and imaging using MIRIAD (Sault et al. 1995).

3. Results

3.1. Continuum Emission

Continuum emission from the nucleus of NGC 6000 was imaged using the CO emission free channels in the USB. The spectral energy distribution (SED) of NGC 6000 shows how most of its continuum emission at 1.3 mm stems from thermal dust emission with no significant evidence of free-free contribution (Roche & Chandler 1993). In Fig. 1 (*left panel*) we show the 1.3 mm continuum emission over the an average image of the J, H, and K 2MASS bands (Skrutskie et al. 2006). The position of the peak of emission at $\alpha_{J2000.0} = 15^{\mathrm{h}}49^{\mathrm{m}}49\overset{\mathrm{s}}{.}5$, $\delta_{J2000.0} = -29°23'13''$ matches that of 2MASS emission within the resolution. This position also matches within $2''$ that of the FIR from low resolution IRAS images (Sanders et al. 2003) and within $1''$ that of the VLA 1.4 GHz peak ($18''$ resolution, Condon et al. 1996). Together with the CO mapping presented in Sect. 3.2, we have obtained the most accurate determination of the nucleus position in NGC 6000, with a resolution better than the $2.5''$ of 2MASS (Skrutskie et al. 2006).

The faint unresolved continuum source has a total flux of 13 ± 3 mJy as measured from our observations. This flux seems to agree with the 18 ± 8 mJy flux observed at 1.3 mm with the $19.5''$ beam of the JCMT telescope (Roche & Chandler 1993). However, the JCMT flux might be overstimated given that the contribution of the CO line (Sect. 3.2) to the continuum in the 64 GHz bolometer band would be ~ 13 mJy. Therefore, the corrected JCMT continuum flux would be a factor of two lower than our measurement. On the other hand, the CO emission would contribute ~ 16 mJy to the 42.7 ± 3.9 mJy average flux measured by the $11''$ beam of the IRAM 30 m over its 50 GHz bolometer band

(Chini et al. 1995). This corrected flux is a factor of two larger than what we recover from our observations. An even larger $1.3\,\mathrm{mm}$ flux of $60.6 \pm 7.8\,\mathrm{mJy}$ was measured by SEST telescope, which is likely due to its larger beam ($24''$) collecting most of the extended emission (Chini et al. 1995). Indeed, the extended $1.3\,\mathrm{mm}$ continuum emission is estimated to be $98\,\mathrm{mJy}$ (CO corrected) in the inner $70''$ with the 5 pointing map observations with the SEST telescope (Albrecht et al. 2007). Assuming the continuum measurements from SEST, we only recovered the compact $\sim 15\%$ of the continuuum emission in our maps.

3.2. Molecular Gas Emission

3.2.1. Comparison to single dish

The total integrated flux recovered from the $^{12}\mathrm{CO}\ 2-1$ image is $1080 \pm 60\,\mathrm{Jy\,km\,s^{-1}}$. Single dish observations of this transition with the $24''$ beam of the SEST telescope resulted in a total detected flux of $780 \pm 80\,\mathrm{Jy\,km\,s^{-1}}$ (Chini et al. 1996), where we assumed a conversion factor of $\sim 25\,\mathrm{Jy/K}$. This difference is contrary to the expected lower flux in the interferometric maps due to filtering of extended emission. Indeed, the $\sim 30\%$ flux difference is too large to be attributed to absolute flux calibration error of both SEST and SMA data. Although SEST observations were taken towards a nominal position $2''$ away from the position of peak emission derived from our map, this difference would only explain a $< 4\%$ lower measured flux. In order to understand this measured flux, we convolved our map to a $24''$ resolution. The asymmetric lineshape in the data from Chini et al. (1996) clearly differs from that obtained at the center of the convolved map and significantly matches the lineshape at a position $\gtrsim 5''$ south of the central position, consistent with the SEST pointing accuracy. This difference in the observing position easily accounts for a difference in the integrated intensity of $> 20\%$ with respect to the central position. Though the uncertain comparison with single-dish data does not allow us to accurately determine

the missed flux in our maps, we can assume that no significant amount of flux have been filtered out and that most of the extended CO emission has been recovered in our maps.

3.2.2. ^{12}CO morphology

The total integrated ^{12}CO $J = 2 - 1$ emission detected in the nuclear region of NGC 6000 is presented in Fig. 1 (*right panel*) on top of the optical HST image (Carollo et al. 1997). In addition to the strong nuclear emission, a fainter extended structure is clearly detected ($> 6\sigma$) extended in the north-south direction, up to a distance of $\sim 12''$ (1.8 kpc) from the center. A similar north-south structure is observed in the near-infrared (Fig. 1, *left panel*).

In Fig. 2 we present the maps of the CO $J = 2 - 1$ integrated emission over the range from 1900 to 2500 km s^{-1} (*Left panel*) and the intensity weighted mean velocities (*Right panel*). The bright nuclear region is just barely resolved by the $2.8'' \times 1.7''$ (430×260 pc) beam. A Gaussian fit to the UV visibilities in the nuclear emission results in a deconvolved extent of $3.7'' \times 2.1''$ (560×320 pc), centered at $\alpha_{J2000.0} = 15^{\mathrm{h}}49^{\mathrm{m}}49{.}^{\mathrm{s}}5$, $\delta_{J2000.0} = -29°23'13''$ (see Table 2). If we assume that the deconvolved ellipticity is due to the inclination of the circumnuclear molecular disk (Sect. 4), an inclination of $31°$ is inferred. This value is in agreement with those derived from large scale images of NGC 6000. The observed position of the CO emission peak matches the derived dynamical center and is in agreement with that derived from the continuum peak. Similar to what is observed in the near-IR 2MASS images, the peak of CO emission does not coincide with the optical peak of emission due to the strong extinction towards the nuclear region. In fact, the extended CO emission follows the dust lanes seen in the optical.

Optical imaging of the nuclear region of NGC6000 shows a bar-like structure with a

nucleus surrounded by an irregular star forming ring with spiral arms down to the ring (Carollo et al. 1997, 2002). Fig. 3 shows the red and blue shifted emission in a close-up view of the central region. The star forming ring structure, offset by $(\alpha, \delta) \sim (-1'', 1'')$ from the peak of molecular emission, appears to be located at the peak of the high velocity CO emission (Fig. 3), right at the eastern edge of the molecular disk. This structure is probably located closer to the observer than the gas disk, and therefore less affected by obscuration. The strongly asymmetrical optical image with respect to the galactic center points to a high extinction, as derived in Section 3.3.2, likely hiding the nuclear and eastern region.

3.2.3. ^{12}CO kinematics

Fig. 4 shows the integrated CO emission over $30 \, \mathrm{km \, s^{-1}}$ channels. The resolved molecular emission in the nuclear region is observed over a range of velocities $\Delta v > 400 \, \mathrm{km \, s^{-1}}$ while the more extended emission is concentrated in the central $\Delta v \sim 300 \, \mathrm{km \, s^{-1}}$. As shown in the channel maps (Fig. 4) the optical bright structures are located at the regions where the most red shifted emission ($v > 2300 \, \mathrm{km \, s^{-1}}$) peaks.

The mean velocity map in Fig. 2 (*Right panel*) shows a strong velocity gradient in the central region, with a smoother variation outside the nucleus. This velocity gradient is clearly shown by the position-velocity (P-V) diagrams shown in Fig. 5. P-V diagrams have been plotted in two different directions, first across the whole molecular emission in the north-south direction (P.A.=0°; left panel in Fig. 5) and second in a direction perpendicular to the axis of rotation of the nuclear region (P.A.=133°; right panel in Fig. 5). Both directions are indicated in the right panel in Fig. 2 as continuous and dashed lines, respectively. The P-V diagrams in both directions show how in the central $4''$ (600 pc) the molecular gas disk is rotating like a rigid-rotor with a rotation velocity $\sim 110 \, \mathrm{km \, s^{-1}}$ per arcsec, equivalent to $0.7 \, \mathrm{km \, s^{-1} \, pc^{-1}}$, after correcting the velocity for an inclination of $\sim 30°$

(Tully 1988; Corwin et al. 1985). This rotation velocity is similar to the average found in the sample of galaxies by Sakamoto et al. (1999) containing barred galaxies like NGC 6000.

3.2.4. ^{13}CO and $C^{18}O$ emission

The emission of the rarer isotopologues were detected towards the nuclear region. Fig. 6 shows the integrated emission of ^{13}CO and C^{18}O compared to that of the main isotopologue. These maps have been natural weighted in order to get a higher sensitivity at the expense of a larger $3.7'' \times 2.2''$ (560×340 pc) beam. The nuclear emission is resolved in both ^{13}CO and C^{18}O in the direction of the disk rotation. However, no extended emission in the north-south direction has been detected in the rarer species due to their much lower abundance and lack of enough sensitivity. Still, the two lowest contours plotted for ^{13}CO appear to be slightly elongated in the same direction as the extended emission traced by ^{12}CO. Gaussian models fitted to the visibilities of each isotopologue give the parameters listed in Table 2. We observe the emission of all the three isotopical substitutions to peak at the same position. The spectrum at the central synthesized beam of each of the natural weighted datacubes is shown in Fig. 7, where the ^{13}CO and C^{18}O spectral features have been multiplied by a factor of 10 for the sake of comparison with the much brighter CO feature.

From our observations we derive an integrated intensity ratio $R^{13}_{2-1} = I[^{12}\mathrm{CO}_{J=2-1}]/I[^{13}\mathrm{CO}_{J=2-1}]$ of ~ 15.5. This ratio is in agreement with those $R^{13}_{1-0} = 11.3 \pm 3.3$ and $R^{13}_{2-1} = 12.7 \pm 4.7$ ratios derived from the CO $J = 1 - 0$ and $J = 2 - 1$ data compilations on normal galaxies with $L_{FIR} < 10^{11}\,L_{\odot}$ (Taniguchi & Ohyama 1998; Taniguchi et al. 1999). The ratio $R^{18}_{2-1} \sim 57.9$ calculated with the C^{18}O isotopologue is similar to those derived for other starburst galaxies (Henkel & Mauersberger 1993). Therefore, assuming the isotopic ratios of ^{12}C/^{13}C$= 40 - 50$ and ^{16}O/^{18}O$= 150 - 200$ apply to NGC 6000, we can estimate an

opacity of the main isotopologue line of $\tau_{CO(2-1)} \sim 2.5 - 5$. We can then accurately assume both ^{13}CO and $C^{18}O$ to be optically thin.

3.3. Mass determination

3.3.1. Dynamical mass

With the derived parameters in Table 2 for central spectra of the CO map we can make a rough estimate of the total dynamical mass within the nuclear region of NGC 6000. The dynamical mass can be calculated as a function of the disk size and the maximum velocity corrected by inclination as $M_{\mathrm{dyn}} = 250\, M_{\odot}\, (V_{max}/sin(i))^2\, R_{\mathrm{d}}$, where the V_{max} and R_{d} are given in $km\, s^{-1}$ and pc, respectively. For this calculation we used the peak velocity of $V_{max} \sim 180\,\mathrm{km\, s^{-1}}$, with respect to the systemic velocity, reached at a distance of $R_{\mathrm{d}} \sim 1.5''$ as measured in the south-east direction of the molecular disk (low velocity end in Fig. 5) so that we avoid the uncertainty due to the disk asymmetry at the higher velocities (Sect. 4). This approximation yields a total mass $M_{dyn} = 7 \times 10^9\, M_{\odot}$.

3.3.2. Mass of molecular gas traced by CO

In order to get an accurate estimate of the mass of molecular hydrogen traced by the carbon monoxide we will use the total flux detected of the isotopologue $C^{18}O$ emission. This is equivalent to using the main isotopologue corrected by opacity effects. Assuming optically thin emission and LTE conditions we can get the mass of hydrogen as

$$N_{\mathrm{H_2}} = (7 \pm 2) \times 10^{18} \frac{[^{12}\mathrm{C}^{16}\mathrm{O}]}{[^{x}\mathrm{C}^{y}\mathrm{O}]} \int T_{\mathrm{b}}^{^{x}\mathrm{C}^{y}\mathrm{O}_{J=2-1}} dv \,\, \mathrm{cm}^{-2} \tag{1}$$

where $^{12}\mathrm{C}^{16}\mathrm{O}/^{x}\mathrm{C}^{y}\mathrm{O}$ is the ratio between the main form of carbon monoxide and any given isotopologue. This expression can be applied for the three isotopologues and

assumes a CO fractional abundance ^{12}CO/H$_2 \sim 8.5 \times 10^{-5}$ (Frerking et al. 1982) and $T_{\mathrm{ex}} = 30 \pm 10\,\mathrm{K}$, similar to the dust temperature derived by Yang & Phillips (2007). Under these conditions, Eq. 1 is equivalent to Eq. 3 in Paglione et al. (2001). With the total flux observed in C^{18}O and the ratio ^{16}O/^{18}O~ 150 (Harrison et al. 1999), we derive an average $N_{\mathrm{H}_2} = (1.0 \pm 0.3) \times 10^{23}\mathrm{cm}^{-2}$. This amount of molecular hydrogen implies a visual extinction of $A_v \sim 100$ magnitudes towards the central region of NGC 6000 which is certainly responsible for the asymmetric optical structure of the nucleus of NGC 6000.

We estimate a total mass of molecular gas in the nuclear region of $M_{\mathrm{H}2} \sim 2.9 \pm 0.9 \times 10^8\,M_\odot$ within the central projected $\sim 566 \times 321\,\mathrm{pc}$ (as measured from the deconvolved CO source size).

From the CO map in Fig. 1 we estimate that $\sim 85\%$ of the molecular mass in NGC 6000 is concentrated in the nuclear $\sim 3''$ region ($\sim 460\,\mathrm{pc}$). This percentage is just a lower limit given the significant opacity affecting the CO emission mostly towards the central peak of emission. Therefore we can estimate a total mass of molecular gas of $3.5 \times 10^8\,M_\odot$ within the inner $\sim 1.8\,\mathrm{kpc}$. Assuming a correction factor 1.36 for the He and heavier elements (Allen 1973), we can estimate a total mass of gas $M_{gas} = 4.6 \times 10^8\,M_\odot$, which yields a ratio $M_{gas}/M_{dyn} \sim 6\%$.

4.   Discussion

4.1.   Bar-driven molecular gas fueling the starburst in NGC 6000

The study of the molecular gas content in a sample of 20 galaxies by Sakamoto et al. (1999) statistically shows that the gas tends to be more concentrated in the central kiloparsec in barred systems. This is the case of NGC 6000 where most of the gas is located in the inner half kiloparsec (Sect. 3.3.2). The large-scale bar revealed in the NIR may also

have a fingerprint in the molecular gas kinematics described in this work. We observe that the P.A.=0° P-V diagram in Fig. 5 (right) shows how the extended molecular component displays a S-shaped feature. This kinematic signature can be understood as the noncircular motions in the context of a barred potential (Binney et al. 1991). The inner material could be moving in the barely resolved x_2 orbits which, with the resolution of our maps, would look like a molecular disk. On the other hand the external gas would be moving in large elliptical x_1 orbits traced as the S-shaped profile in the P-V diagram. Higher resolution imaging of NGC 6000 might support the scenario of a barred potential by resolving the inner disk structure into circular x_2 orbits as observed by Meier et al. (2008) towards Maffei 2. Similar signatures of a barred potential are observed in the P-V diagrams of other galaxies such as NGC 1530 and NGC 4258 (Downes et al. 1996; Cox & Downes 1996) and equivalent structure are found in their innermost regions.

However our measured M_{gas}/M_{dyn} ratio of 6% is lower than the average measured by Sakamoto et al. (1999) in starbursts and barred galaxies. This measurement is significantly affected by the way the gas mas is calculated Indeed, adopting their same conversion factor ($X = 3 \times 10^{19}\,\mathrm{cm}^{-2}(\mathrm{K\,km\,s}^{-1})^{-1}$ rather than $X = 0.4 \times 10^{19}\,\mathrm{cm}^{-2}(\mathrm{K\,km\,s}^{-1})^{-1}$, see Sect. 4.3) the measured ratio would increase up to $\sim 35\%$. This ratio is only found in barred starbursts in the Sakamoto et al. (1999) sample.

4.2. The high velocity asymmetry

The strong asymmetry in the nuclear ring/disk is also a particularly interesting feature. As seen in Fig. 5 a significant part of the molecular gas traced by CO is skewed towards the region at the lowest velocities, corresponding to the south-east disk component. However, the emission at the highest velocities from 2300 to 2400 $\mathrm{km\,s}^{-1}$ in the P-V diagrams, although following the same rotation gradient, seems to be significantly detached from the

inner rotating structure. This feature at the highest velocities corresponds to the wing observed in the spectrum shown in Fig. 7. We discard the possibility of self-absoption at high velocities, which would change the systemic velocity derived from the Gaussian fit to the line, as the optically thin ^{13}CO and C^{18}O show similar profiles and are centered at the same velocity. It is surprising that ^{13}CO and even C^{18}O are detected in this velocity component between 2300 to $2400\,\mathrm{km\,s^{-1}}$. Moreover, the low ratio of ^{13}CO and C^{18}O with respect to the main isotopologue implies that a significant opacity is affecting even the ^{13}CO emission in this molecular component. CO being optically thick can provide some constraint on the extent of the emission as compared to our resolution. From the CO brightness temperature measured $T_{\mathrm{b}} \sim 1\,\mathrm{K}$ and assuming an excitation temperature $T_{\mathrm{ex}} = 30\,\mathrm{K}$ (as derived from the dust temperature, Yang & Phillips 2007, and assuming CO being thermalized at this temperature), we estimate the region extent to be $< 80\,\mathrm{pc}$ ($< 0.5''$). This is slightly above the $\sim 50\,\mathrm{pc}$ typical size of giant molecular clouds within our Galaxy. This giant molecular cloud within the inner region of NGC 6000 must be very dense and more compact than our estimate to explain such CO opacity. It could have originated as a shock between the circumnuclear disk and the infalling molecular gas along the dust lanes. Moreover, emission arises from the same region as the star forming ring which suggest that this dense and compact molecular cloud might be directly related to the fueling of star formation event in this region.

4.3. CO-to-H$_2$ conversion factor in starburst galaxies

We can estimate the column density of molecular gas via the conversion factor $X = N(H_2)/CO = 3.0 \times 10^{20}\,\mathrm{cm^{-2}}(\mathrm{K\,km\,s^{-1}})^{-1}$ based on measurements of galactic disk molecular clouds (Solomon et al. 1987). This way, and adopting the CO integrated intensity in this work, we derive a H$_2$ column density of $7.5 \times 10^{23}\mathrm{cm^{-2}}$ which is almost

an order of magnitude larger than the value derived from the optically thin $C^{18}O$ line (Sect. 3.3.2). As already observed towards the starburst NGC 253 (Mauersberger et al. 1996; Harrison et al. 1999), the conversion factor in the starburst environment might be significantly lower than that in the Galactic disk. From our measurements we calculate a conversion factor $X = 0.4 \times 10^{19} \, \text{cm}^{-2} (\text{K km s}^{-1})^{-1}$ in agreement with that derived for NGC 253 (Mauersberger et al. 1996). This result support the evidences found for a lower conversion factor in the central region of galaxies, and in particular in starburst with respect to the Galactic disk (Downes & Solomon 1998) or that measured in star forming regions in the Large Magellanic Clouds (Wang et al. 2009).

5. Summary

We have obtained high resolution $(2.8'' \times 1.7'')$ maps of the molecular emission towards NGC 6000 as traced by the $J = 2 - 1$ transition of carbon monoxide with the SMA. Emission from the three main isotopologues of carbon monoxide, ^{12}CO, ^{13}CO, and $C^{18}O$ are detected. Both the continuum and molecular emission peak at the same position. From these measurements we have accurately determined the nucleus position in NGC 6000 at $\alpha_{J2000.0} = 15^h49^m49\overset{s}{.}5$ and $\delta_{J2000.0} = -29°23'13$, in agreement with previous IR determinations. More than an 85% of the emission is concentrated towards the nuclear projected $\sim 400 \times 300 \, \text{pc}$ region, where we estimate optical extinctions of the order of ~ 100 magnitudes. Such large obscuration is likely responsible for the asymmetry in the optical images, probably hiding the eastern part of the nuclear region at these wavelengths.

The emission from the central region is resolved in the direction of the observed velocity gradient. Molecular emission is detected in the north-south direction extended up to distances of $> 1.5 \, \text{kpc}$ from the center. However this is only detected in the main isotopologue. Both the nuclear and extended emission show dynamical evidences that might

be explained by the presence of a bar potential affecting the molecular material, likely responsible of the strong nuclear concentration and maybe the starburst event. We observed a high velocity component which appears to be detached from the nuclear disk/ring and is highly optically thick. With an estimated extent of $< 80\,\mathrm{pc}$, this giant molecular cloud is likely to be related to the fueling of the nuclear star burst in NGC 6000.

The ratios of ^{13}CO and C^{18}O with respect to the main isotopologue are similar to the average measured in similar starburst galaxies with luminosities $L_{FIR} < 10^{11} L_{\odot}$ in the literature (Henkel & Mauersberger 1993).

The total dynamical mass derived for NGC 6000 is $1.9 \times 10^9\, M_{\odot}$. We estimate a total mass of molecular gas of $4.6 \times 10^8 M_{\odot}$ and a ratio $M_{gas}/M_{dyn} \sim 6\%$, similar to the starbursts in the barred galaxy sample by (Sakamoto et al. 1999). The independent estimate of the molecular mass with the optically thin C^{18}O isotope allows the determination of the conversion factor CO-to-H2 of $X_{CO} = 0.4 \times 10^{19}\,\mathrm{cm}^{-2}(\mathrm{K\,km\,s}^{-1})^{-1}$, which agrees with previous estimates that measure a lower factor in starburst nuclear regions (Mauersberger et al. 1996) as compared with the standard factor derived for Galactic disk clouds.
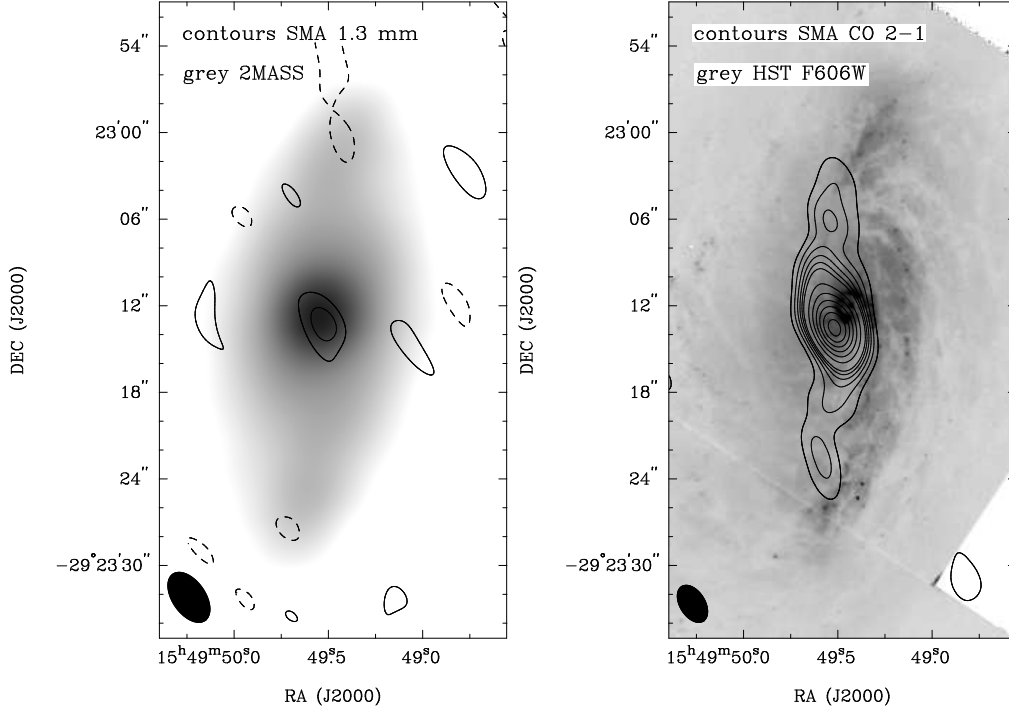
Facilities: SMA ()

Fig. 1.— *Left panel:* 1.3 mm continuum natural weighted emission in NGC 6000 as measured with the SMA (contours) over an average of the J, H, and K 2MASS (grey scale Skrutskie et al. 2006). Contours levels are 2σ significant as -5, 5, and 10 mJy. 2MASS image is displayed in logarithmic scale. *Right panel:* Composite image of the uniform weighted ^{12}CO $J = 2 - 1$ integrated emission (contours) and the optical HST-WFPC2 image in the F606W filter of NGC 6000 (Carollo et al. 1997). Contours are 3σ levels from 12 to 74 Jy beam^{-1} km s^{-1} and 10σ from 115 to 445 Jy beam^{-1} km s^{-1}, where $\sigma = 4.1$ Jy/beam km s^{-1} in the image. HST image is displayed in logarithmic scale. The respective synthesized beams of each map are displayed in the bottom left-hand corner of each plot.
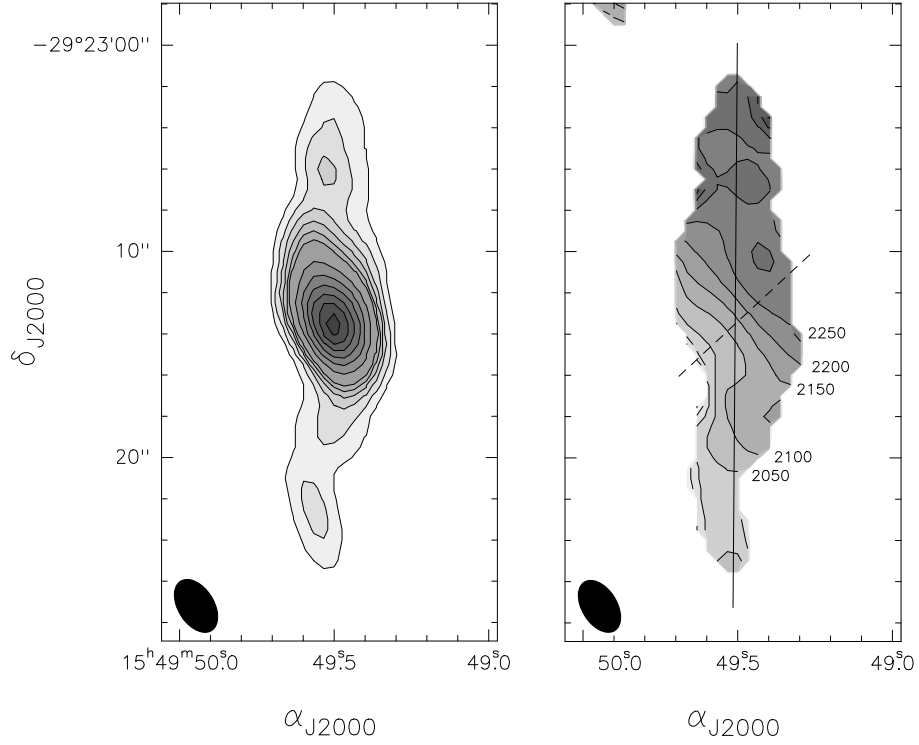
Fig. 2.— ^{12}CO $J = 2 \to 1$ integrated emission and kinematics towards the nuclear region of NGC 6000. The synthesized beam of the uniform weighted maps $(2.8'' \times 1.7'')$ is plotted at the bottom left-hand corner of each plot. *Left panel:* Integrated flux over the velocity range of 1900 and 2500 km s^{-1}. Contours are similar to those used in Fig. 1. *Right panel:* Mean velocity field map. Contours are uniformly spaced by 50 km s^{-1}. Only pixel above 3σ level in integrated intensity map are shown. The solid and dashed lines are the cut directions used for the position-velocity diagrams in Fig. 5.
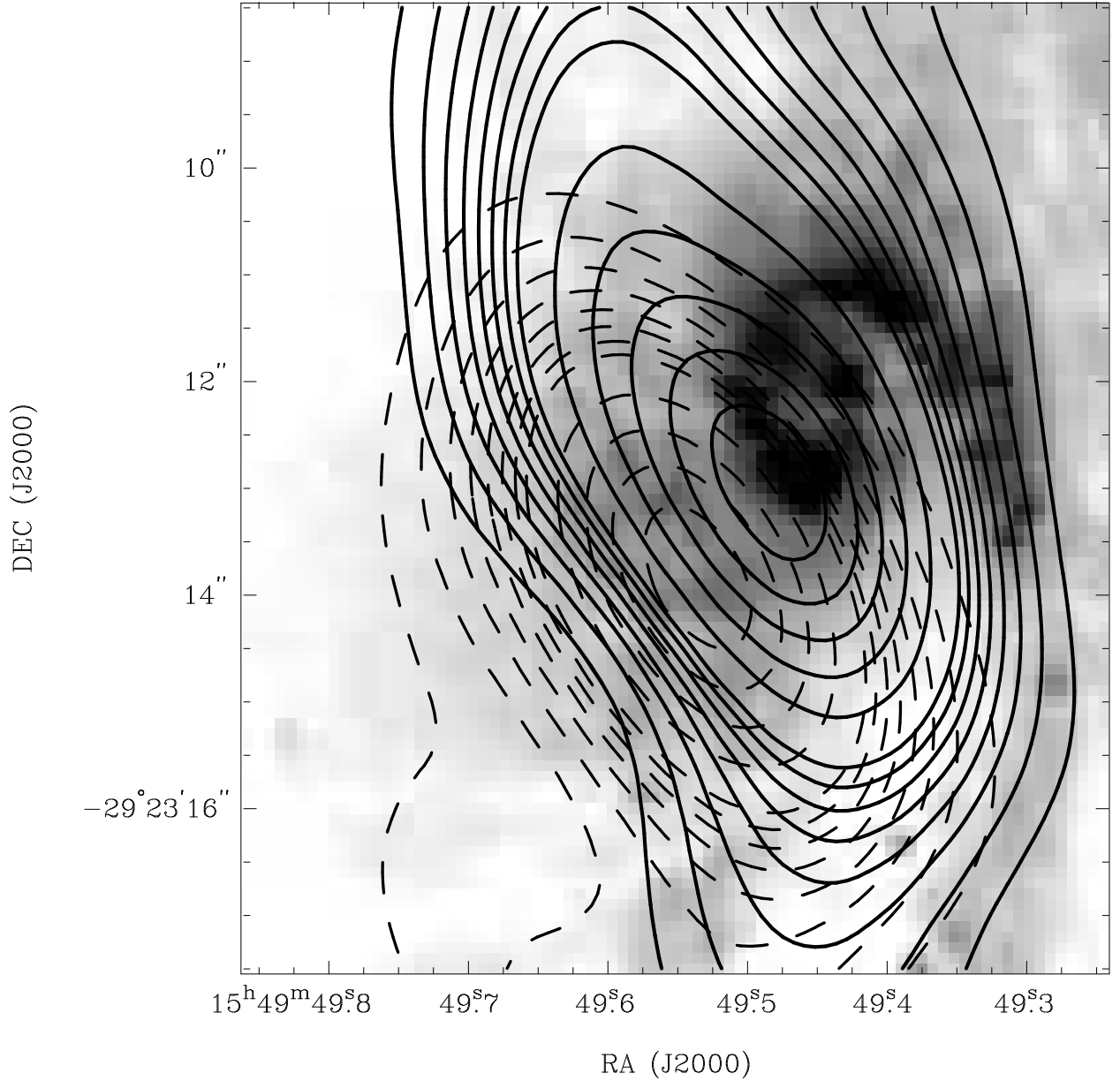
Fig. 3.— Close-up image of the central region of NGC 6000. The CO red (solid contours) and blue shifted (dashed contours) emission are plotted over the optical HST-WFPC2 image (Carollo et al. 1997). Emission has been integrated -250 and $+250\,\mathrm{km\,s^{-1}}$ with respect to the systemic velocity ($2135\,\mathrm{km\,s^{-1}}$) for the blue and red shifted components, respectively. Contours are 3σ levels from 7.5 to $60\,\mathrm{Jy\,km\,s^{-1}}$ and 10σ from 60 to $185\,\mathrm{Jy\,km\,s^{-1}}$, where $\sigma \sim 2.5\,\mathrm{Jy/beam\,km\,s^{-1}}$ in both images. The optical emission is strongly asymmetrical with respect to the dynamical center. We observe that the star forming ring, significantly offset from the center of the galaxy, is located at the position where the highest velocity CO emission is observed as better seen in the channel maps in Fig. 4.
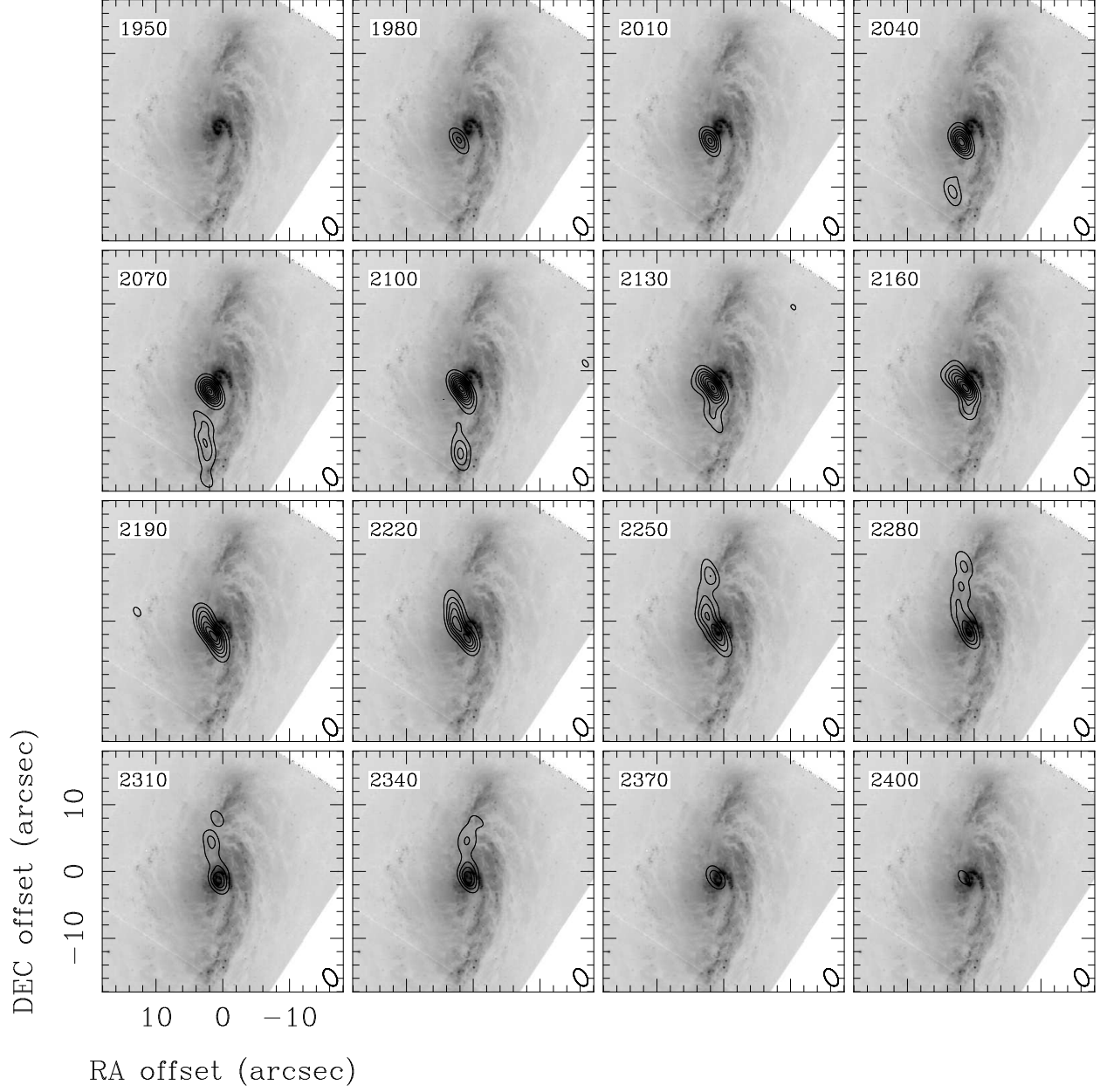
Fig. 4.— ^{12}CO channel maps (Contours) in steps of $30\,\mathrm{km\,s^{-1}}$ plotted over the HST-WFPC2 image (Carollo et al. 1997). Contours are plotted at 2σ levels of $1.8\,\mathrm{Jy\,km\,s^{-1}}$. Central velocity of each channel is shown in the upper left corner and beam size in the lower right.
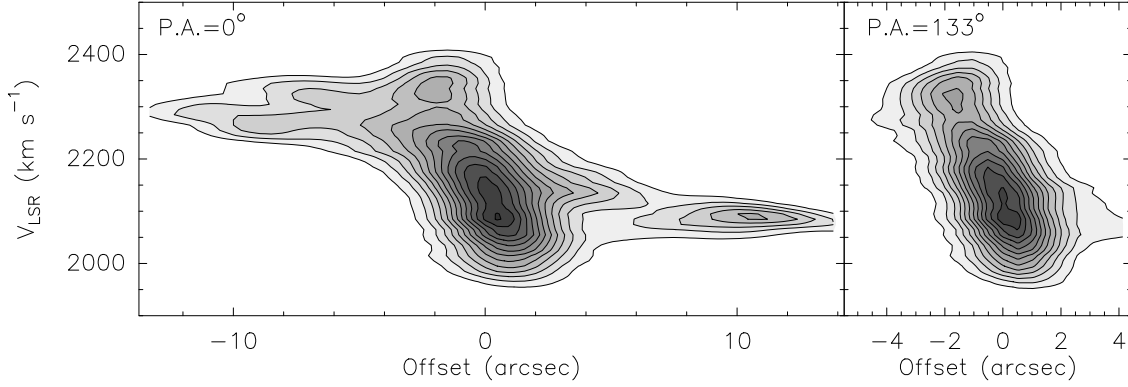
Fig. 5.— Position-Velocity diagrams across the nuclear region of NGC 6000 in the P.A.=0°
and P.A.=133° directions. Contours are 6σ levels (0.15 Jy) from 0.15 Jy to 1.95 Jy. Both
cuts directions are shown in Fig. 2 by the solid and dashed lines, respectively.
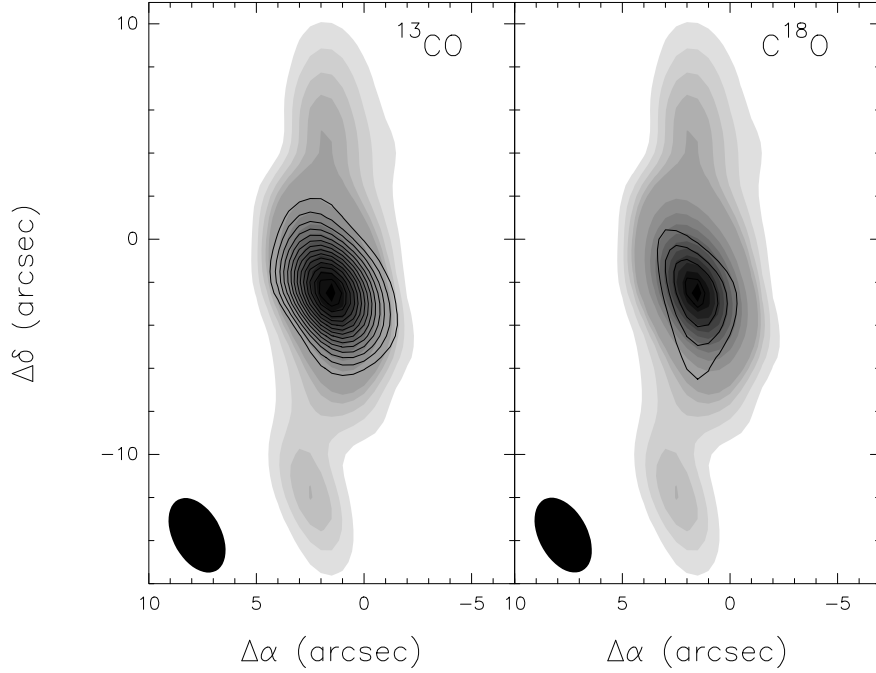

Fig. 6.— Natural weighted integrated flux maps of the observed $J = 2 \rightarrow 1$ transition in
the different CO isotopologues (contours), compared to the ^{12}CO emission (grey scale). The
beam size in these maps is $3.7'' \times 2.2''$ (shown as filled ellipses at the bottom left corner). ^{12}CO
grey scale levels corresponds to those in Fig. 2. Contours are 2σ levels (4.4 Jy beam^{-1} km s^{-1})
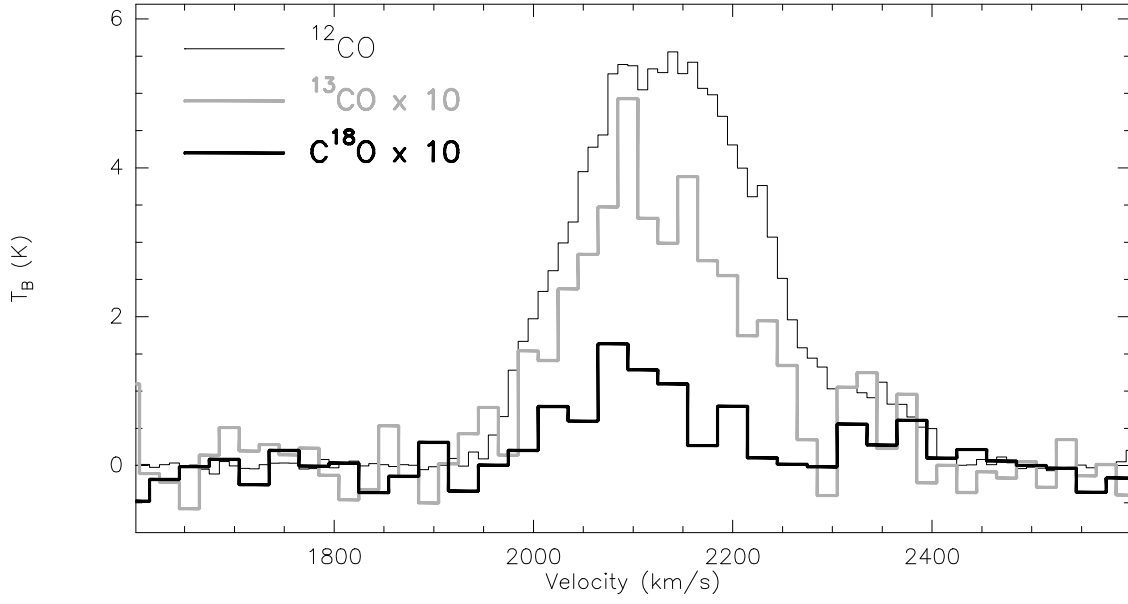in both ^{13}CO and C^{18}O.

Fig. 7.— Brightness temperature spectra of the three isotopologues extracted from the central synthesized beam of the natural weighted datacubes. The resolution in velocity is of $10\,\mathrm{km\,s^{-1}}$ for the main isotope, $20\,\mathrm{km\,s^{-1}}$ for ^{13}CO, and $30\,\mathrm{km\,s^{-1}}$ for C^{18}O. The spectra of ^{13}CO and C^{18}O has been multiplied by a factor of 10 for the sake of clarity in the comparison.

Table 1.   Summary of observational parameters for NGC 6000

Parameter	Value	Reference
GALAXY POSITION		
ROSAT (J2000)	15:49:50.1, -29:23:10.7	1
IRAS (J2000)	15:49:49.4, -29:23:11	2
V_{LSR}	$2145\,\mathrm{km\,s^{-1}}$	3
Distance ($H_0 = 75\,km\,s^{-1}\,Mpc^{-1}$)	$31.6\,\mathrm{Mpc}$	4
MORPHOLOGY		
Morphological type	SB(s)bc	5
Inclination	$33°$, $27°$	6,7
log D_{25} $(0.1')$	1.27	5
Weighted mean luminosity class	4.0	7
$Diameter_{maj\times min}$	$2.3' \times 2.0'$	8
P.A.	$154°,163°$	5,9
PHYSICAL PARAMETERS		
T$_{dust}$ (K)	34, 30	10,11
$M_{dust}\,(M_\odot)$	1.5×10^9, 2.4×10^7	10,11
log $L_{FIR}\,(\,L_\odot)$	10.83	12
log $L_{IR}\,(\,L_\odot)$	10.97	12
log $M_{HI}\,(M_\odot)$	9.86, 9.8	13,14
log $M_{H2}\,(M_\odot)$	8.5	15
log $M_{gas}\,(M_\odot)$	8.7, 10.0	15,16
log $M_{dyn}\,(M_\odot)$	9.8	15

References.   — (1) Boller et al. 1992; (2) Sanders et al. 2003; (3) Albrecht et al. 2007; (4) Pizzella et al. 2005; (5) de Vaucouleurs et al.

1991; (6) Tully 1988; (7) Corwin et al. 1985; (8) Dressler 1991; (9) Young et al. 1995; (10) Roche & Chandler 1993; (11) Yang & Phillips 2007; (12) Sanders et al. 2003; (13) Martin et al. 1991; (14) Koribalski et al. 2004; (15) This work; (16) Chini et al. 1995;

Table 2.   Derived parameters from the CO, ^{13}CO and C^{18}O observed emission

Parameter	CO	^{13}CO	C^{18}O
	Gaussian fit to the maps [a]		
Center (J2000.0)	15:49:49.5, -29:23:13	15:49:49.5, -29:23:13	15:49:49.5, -29:23:13
Size (FWHM)	$3.7'' \times 2.1''$, P.A. 12°	$2.7'' \times 2.1''$, P.A. 29°	$2.5'' \times 1.3''$, P.A. 5°
Total Flux	922 ± 9 Jy km s^{-1}	90 ± 7 Jy km s^{-1}	33 ± 6 Jy km s^{-1}
	Central pixel spectra [b]		
V_{LSR}	2135.3 ± 0.3 km s^{-1}	2119 ± 4 km s^{-1}	2104 ± 9 km s^{-1}
$\Delta v_{1/2}$	217.1 ± 0.6 km s^{-1}	196 ± 10 km s^{-1}	150 ± 20 km s^{-1}
T_{B}	5600 mK	400 mK	140 mK

[a]Results of the deconvolved Gaussian fit models applied to the UV visibilities.

[b]Parameters from the Gaussian fit to the spectra at the central pixel of each map.

REFERENCES

Albrecht, M., Krügel, E., & Chini, R. 2007, A&A, 462, 575

Allen, C. W. 1973, Astrophysical quantities, ed. C. W. Allen

Binney, J., Gerhard, O. E., Stark, A. A., Bally, J., & Uchida, K. I. 1991, MNRAS, 252, 210

Boller, T., Meurs, E. J. A., Brinkmann, W., Fink, H., Zimmermann, U., & Adorf, H.-M. 1992, A&A, 261, 57

Carollo, C. M. 1999, ApJ, 523, 566

Carollo, C. M., Stiavelli, M., de Zeeuw, P. T., & Mack, J. 1997, AJ, 114, 2366

Carollo, C. M., Stiavelli, M., Seigar, M., de Zeeuw, P. T., & Dejonghe, H. 2002, AJ, 123, 159

Chini, R., Kruegel, E., & Lemke, R. 1996, A&AS, 118, 47

Chini, R., Kruegel, E., Lemke, R., & Ward-Thompson, D. 1995, A&A, 295, 317

Condon, J. J., Helou, G., Sanders, D. B., & Soifer, B. T. 1996, ApJS, 103, 81

Corwin, H. G., de Vaucouleurs, A., & de Vaucouleurs, G. 1985, University of Texas Monographs in Astronomy, 4, 1

Cox, P., & Downes, D. 1996, ApJ, 473, 219

de Vaucouleurs, G., de Vaucouleurs, A., Corwin, Jr., H. G., Buta, R. J., Paturel, G., & Fouque, P. 1991, Third Reference Catalogue of Bright Galaxies (Volume 1-3, XII, 2069 pp. 7 figs.. Springer-Verlag Berlin Heidelberg New York)

Downes, D., Reynaud, D., Solomon, P. M., & Radford, S. J. E. 1996, ApJ, 461, 186

Downes, D., & Solomon, P. M. 1998, ApJ, 507, 615

Dressler, A. 1991, ApJS, 75, 241

Fathi, K., & Peletier, R. F. 2003, A&A, 407, 61

Frerking, M. A., Langer, W. D., & Wilson, R. W. 1982, ApJ, 262, 590

Harrison, A., Henkel, C., & Russell, A. 1999, MNRAS, 303, 157

Henkel, C., & Mauersberger, R. 1993, A&A, 274, 730

Ho, P. T. P., Moran, J. M., & Lo, K. Y. 2004, ApJ, 616, L1

Hunt, L. K., & Malkan, M. A. 2004, ApJ, 616, 707

Jogee, S., Scoville, N., & Kenney, J. D. P. 2005, ApJ, 630, 837

Knapen, J. H., Pérez-Ramírez, D., & Laine, S. 2002, MNRAS, 337, 808

Koribalski, B. S., Staveley-Smith, L., Kilborn, V. A., Ryder, S. D., Kraan-Korteweg, R. C., Ryan-Weber, E. V., Ekers, R. D., Jerjen, H., Henning, P. A., Putman, M. E., Zwaan, M. A., de Blok, W. J. G., Calabretta, M. R., Disney, M. J., Minchin, R. F., Bhathal, R., Boyce, P. J., Drinkwater, M. J., Freeman, K. C., Gibson, B. K., Green, A. J., Haynes, R. F., Juraszek, S., Kesteven, M. J., Knezek, P. M., Mader, S., Marquarding, M., Meyer, M., Mould, J. R., Oosterloo, T., O'Brien, J., Price, R. M., Sadler, E. M., Schröder, A., Stewart, I. M., Stootman, F., Waugh, M., Warren, B. E., Webster, R. L., & Wright, A. E. 2004, AJ, 128, 16

Martin, J. M., Bottinelli, L., Gouguenheim, L., & Dennefeld, M. 1991, A&A, 245, 393

Mauersberger, R., Henkel, C., Walsh, W., & Schulz, A. 1999, A&A, 341, 256

Mauersberger, R., Henkel, C., Wielebinski, R., Wiklind, T., & Reuter, H.-P. 1996, A&A, 305, 421

Meier, D. S., Turner, J. L., & Hurt, R. L. 2008, ApJ, 675, 281

Paglione, T. A. D., Wall, W. F., Young, J. S., Heyer, M. H., Richard, M., Goldstein, M., Kaufman, Z., Nantais, J., & Perry, G. 2001, ApJS, 135, 183

Pérez-Ramírez, D., Knapen, J. H., Peletier, R. F., Laine, S., Doyon, R., & Nadeau, D. 2000, MNRAS, 317, 234

Pfenniger, D., & Norman, C. 1990, ApJ, 363, 391

Pizzella, A., Corsini, E. M., Dalla Bontà, E., Sarzi, M., Coccato, L., & Bertola, F. 2005, ApJ, 631, 785

Roche, P. F., & Chandler, C. J. 1993, MNRAS, 265, 486

Sakamoto, K., Okumura, S. K., Ishizuki, S., & Scoville, N. Z. 1999, ApJ, 525, 691

Sanders, D. B., Mazzarella, J. M., Kim, D.-C., Surace, J. A., & Soifer, B. T. 2003, AJ, 126, 1607

Sault, R. J., Teuben, P. J., & Wright, M. C. H. 1995, in ASP Conf. Ser. 77: Astronomical Data Analysis Software and Systems IV, ed. R. A. Shaw, H. E. Payne, & J. J. E. Hayes, 433

Sheth, K., Vogel, S. N., Regan, M. W., Thornley, M. D., & Teuben, P. J. 2005, ApJ, 632, 217

Siebenmorgen, R., Krügel, E., & Spoon, H. W. W. 2004, A&A, 414, 123

Skrutskie, M. F., Cutri, R. M., Stiening, R., Weinberg, M. D., Schneider, S., Carpenter, J. M., Beichman, C., Capps, R., Chester, T., Elias, J., Huchra, J., Liebert, J., Lonsdale, C., Monet, D. G., Price, S., Seitzer, P., Jarrett, T., Kirkpatrick, J. D., Gizis, J. E., Howard, E., Evans, T., Fowler, J., Fullmer, L., Hurt, R., Light, R., Kopan, E. L., Marsh, K. A., McCallon, H. L., Tam, R., Van Dyk, S., & Wheelock, S. 2006, AJ, 131, 1163

Solomon, P. M., Rivolo, A. R., Barrett, J., & Yahil, A. 1987, ApJ, 319, 730

Taniguchi, Y., & Ohyama, Y. 1998, ApJ, 507, L121

Taniguchi, Y., Ohyama, Y., & Sanders, D. B. 1999, ApJ, 522, 214

Tully, R. B. 1988, Nearby galaxies catalog (Cambridge and New York, Cambridge University Press, 1988, 221 p.)

Wang, M., Chin, Y.-N., Henkel, C., Whiteoak, J. B., & Cunningham, M. 2009, ApJ, 690, 580

Yang, M., & Phillips, T. 2007, ApJ, 662, 284

Young, J. S., Xie, S., Tacconi, L., Knezek, P., Viscuso, P., Tacconi-Garman, L., Scoville, N., Schneider, S., Schloerb, F. P., Lord, S., Lesser, A., Kenney, J., Huang, Y.-L., Devereux, N., Claussen, M., Case, J., Carpenter, J., Berry, M., & Allen, L. 1995, ApJS, 98, 219